RSC Advances

PAPER

Cite this: *RSC Adv.*, 2014, **4**, 59981

One-step solvothermal preparation of Fe_3O_4/graphene composites at elevated temperature and their application as anode materials for lithium-ion batteries

Laiying Jing,[a] Aiping Fu,[a] Hongliang Li,*[a] Jingquan Liu,[a] Peizhi Guo,*[a] Yiqian Wang[b] and Xiu Song Zhao[ac]

A one-step high-temperature solvothermal process (can be used up to 400 °C) has been explored for the preparation of Fe_3O_4/graphene composites. The influence of high temperature (>230 °C) on the structure, morphology and electrochemical properties of the resulting Fe_3O_4/graphene composites was investigated by XRD, SEM, TEM and N_2 adsorption–desorption measurements. Electrochemical performances of the as-prepared Fe_3O_4/graphene composites at different temperatures were evaluated in coin-type cells as anode materials for lithium-ion batteries. In comparison with the traditional solvothermal method (<240 °C), the high-temperature method does not require an additional calcination process yet it still could result in Fe_3O_4/graphene composites with pure phase and excellent electrochemical properties. A preferred solvothermal temperature of 280 °C has been deduced based on a series of control experiments. The Fe_3O_4/graphene composite derived at 280 °C exhibited a high reversible capacity of 907 mA h g^{-1} at 0.1 C (92.6 mA g^{-1}) even after 65 cycles, showing outstanding cycle stability. It also exhibited a high rate capability of 410 mA h g^{-1} at 2 C (1852 mA g^{-1}). The role of the graphene substrates in improving the electrochemical properties of the composite is discussed based on the morphology, structure, phase and electrochemical property studies.

Received 22nd August 2014
Accepted 31st October 2014

DOI: 10.1039/c4ra09079a

www.rsc.org/advances

1. Introduction

Recently, lithium-ion batteries (LIBs) have generated great interest because of the impact of portable electronic devices. Transition metal oxides have been considered as promising high-performance anode materials for LIBs due to their high energy density, safety for diverse applications, environmental friendliness and low cost.[1–6] Among the transition metal oxides, magnetite (Fe_3O_4) is the most promising candidate anode material for LIBs because of its higher theoretical reversible capacity (926 mA h g^{-1}) in comparison with carbonaceous substances.[7–10] However, the low initial coulombic efficiency and the severe volume changes during the Li ion insertion/extraction processes lead to a poor cycling performance, limiting the commercialization of this potential material.[11–14] Hence, a flexible strategy for improving the reversible capacity and long-cycle performance has been of significant interest in developing high-performance LiB anode materials. Graphene is a one-atom thick planar sheet in a honeycomb crystal lattice and has been extensively explored as conductive materials for energy storage.[15,16] Graphene/Fe_3O_4 composites with excellent LIB performance have also been reported.[17–19] Graphene shows three main advantages as conductive substrates for the fabrication of composite electrode materials. Firstly, the sheets can provide voids against the volume changes of the Fe_3O_4 particles during the Li ion insertion/extraction processes.[20–22] Secondly, graphene sheets can prevent the aggregation of Fe_3O_4 particles by the lamellar structure. Thirdly, it also can improve the rate performance of the composites due to its intrinsic high electronic conductivity. In the previous studies, most of the graphene/Fe_3O_4 composites were prepared by hydrothermal or solvothermal methods at a temperature below 200 °C due to the limitation of the Teflon liner (the softening point of the polytetrafluoroethylene autoclave liner is 240 °C). Usually, the normal solvothermal process necessitates a long reaction time (more than 12 h and even several days) and requires a subsequent calcination step at temperatures higher than 500 °C to obtain transition metal oxide based composite materials with pure phase and excellent electrochemical properties.[23–25] One question then arises: what will happen when the solvothermal

[a]*Collaborative Innovation Center for Marine Biomass Fibers, Laboratory of New Fiber Materials and Modern Textile, Growing Base for State Key Laboratory, College of Chemical Science and Engineering, Qingdao University, Qingdao 266071, China. E-mail: lhl@qdu.edu.cn; pzguo@qdu.edu.cn; Tel: +86-532-85950767*

[b]*College of Physics, Qingdao University, No. 308 Ningxia Road, Qingdao, 266071, China*

[c]*School of Chemical Engineering, The University of Queensland, St Lucia, Brisbane, QLD 4072, Australia*

preparation of transition metal oxide is conducted at a temperature higher than 240 °C? However, it is difficult to find an answer in the literature due to the temperature limitation of normal structured autoclaves.

Attempting to address the above question and to exploit new techniques, a one-step high-temperature solvothermal approach (up to 310 °C) for the preparation of Fe_3O_4/graphene composites has been explored herein based on a Swagelok structured autoclave using an organic iron(II) compound as precursor. Fe_3O_4/graphene composites with high reversible capacity and outstanding cycle stability have been prepared within 6 h *via* this high-temperature solvothermal process and no further calcinations were needed. The influence of treatment temperature and reaction time on the composition, structure, morphology and electrochemical properties of the resultant Fe_3O_4/graphene composites were investigated in detail.

2. Experimental section

2.1. Materials

Ferrous oxalate dihydrate, ferric chloride hexahydrate, anhydrous sodium acetate and ethylene glycol (Sinopharm Chemical Reagent Co., Ltd) were of AR grade and used without further purification. Graphene, kindly provided by the sixth element (Changzhou) Ltd, was used as received without further treatment.

2.2. Synthesis of Fe_3O_4/graphene composites

The Fe_3O_4/graphene composites were synthesized by a simple one-step high-temperature solvothermal process. Typically, 0.32 g of ferrous oxalate dihydrate, 0.2 g of anhydrous sodium acetate and 0.011 g of graphene were added to 5 mL of ethylene glycol under vigorous stirring. After stirring for 20 min, the mixture was transferred into a Swagelok structured stainless autoclave with a capacity of 8 mL (a homemade stainless steel (316) high-pressure cell with a Swagelok fitting was used to maintain the pressure at high temperatures up to 400 °C). Then the autoclave was put into a thermostatic oven for solvothermal treatment for 6 or 12 h at different temperatures (210, 230, 250, 280 or 310 °C). After the autoclave had cooled down to room temperature naturally, black precipitates were collected after centrifugation. The solids were washed with distilled water and ethanol twice, respectively, and then dried at 60 °C in a thermostatic oven, obtaining about 0.12 g Fe_3O_4/graphene composite with a reproducible yield of 85% calculated based on ferrous oxalate dihydrate. The resultant composites prepared under different temperatures were designated as Fe_3O_4/graphene (T °C) in the following discussion (where T = 210, 230, 250, 280 or 310 °C, respectively, corresponding to the applied treating temperatures). An illustration of the formation process of the Fe_3O_4/graphene composites is illustrated in Scheme 1. For comparison purposes, Fe_3O_4 nanoparticles were prepared in the same way as that of Fe_3O_4/graphene but in the absence of graphene. As a control experiment, the Fe_3O_4/graphene composite was also prepared using the traditional solvothermal method at 200 °C for 12 h using ferric chloride hexahydrate as precursor.[26]

Scheme 1 Illustration of the formation process of the Fe_3O_4/graphene composites.

2.3. Characterization

The crystallographic information and composition of the products were investigated using a Bruker D8 advance X-ray diffractometer (XRD, Cu-Kα radiation λ = 0.15418). Fourier transform infrared spectra were recorded from 400 to 4000 cm^{-1} with a Nicolet 5700 spectrophotometer using pressed KBr pellets. Raman spectra were collected using a Horiba LabRAM HR Raman spectrometer (HORIBA Jobin Yvon Ltd.). The carbon content in the composites was determined by thermogravimetric analysis under an oxygen atmosphere with a heating rate of 10 °C min^{-1} (Mettler Toledo TGA/STDA851^e). The morphologies and the structures of the samples were examined by a JEOL JSM-6390LV scanning electron microscope (SEM) and a JEOL JEM-2010F transmission electron microscope (TEM). The specific surface areas were estimated with the Brunauer–Emmett–Teller (BET) method with N_2 adsorption data in the relative pressure range of P/P_0 = 0.05–0.35. The pore size distributions were calculated using the Barrett–Joyner–Halenda (BJH) model applied to the desorption branch of the N_2 isotherms obtained with a TriStar 3000 surface area and pore analyzer (Micromeritics).

2.4. Electrochemical testing

The working electrodes were prepared by mixing the active material, acetylene black (super-P) and polyvinylidene fluoride

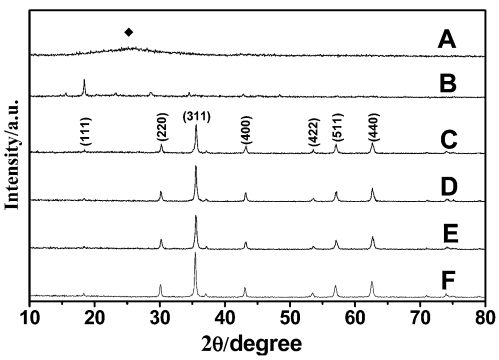

Fig. 1 XRD patterns of graphene (A), Fe_3O_4/graphene (210 °C) (12 h) (B), Fe_3O_4/graphene (230 °C) (12 h) (C), Fe_3O_4/graphene (250 °C) (12 h) (D), Fe_3O_4/graphene (280 °C) (6 h) (E), and Fe_3O_4 (280 °C) (12 h) (F).

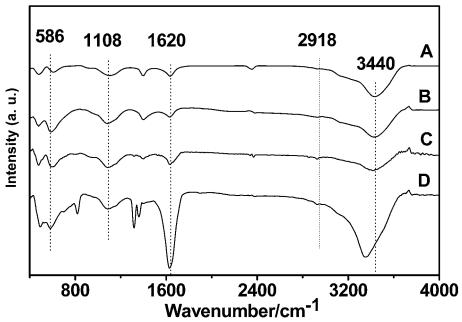

Fig. 2 FTIR spectra of graphene (A), Fe_3O_4/graphene (280 °C) (B), Fe_3O_4/graphene (250 °C) (C), Fe_3O_4/graphene (230 °C) (D).

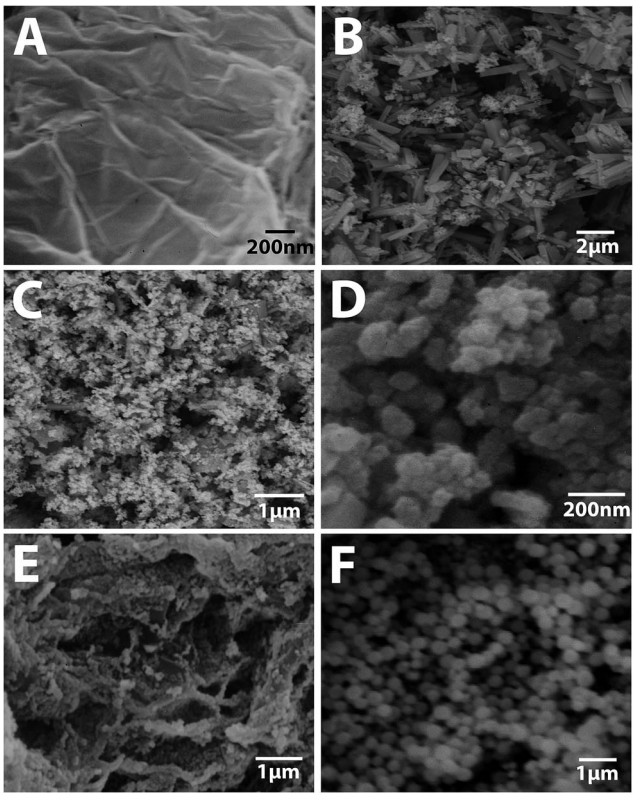

Fig. 3 SEM images of graphene (A), Fe_3O_4 nanoparticles (230 °C) (B), Fe_3O_4 nanoparticles (250 °C) (C), Fe_3O_4 nanoparticles (280 °C) (D), Fe_3O_4/graphene composite (280 °C) (E) and Fe_3O_4/graphene composite prepared *via* the traditional solvothermal method using ferric chloride hexahydrate as precursor (F).

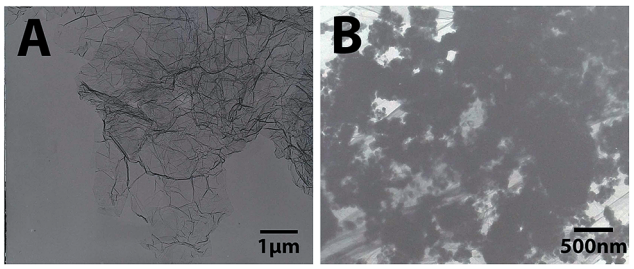

Fig. 4 TEM images of the graphene substrate (A), and Fe_3O_4/graphene (280 °C) composite (B).

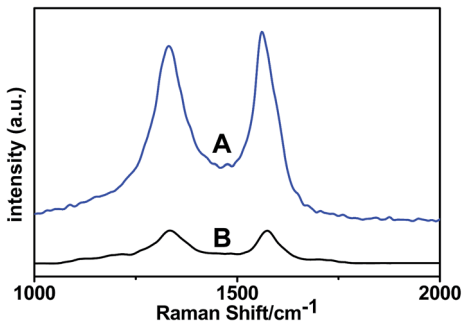

Fig. 5 Raman spectra of graphene substrate (A) and that of Fe_3O_4/graphene (280 °C) composite (B).

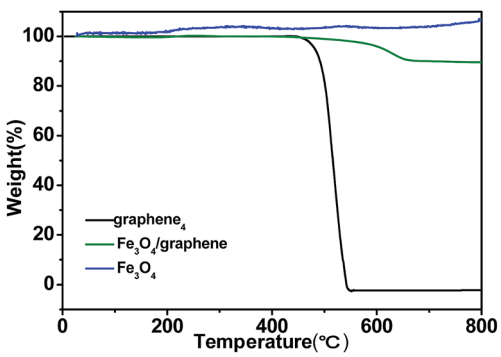

Fig. 6 TGA profiles of pristine graphene, pure Fe_3O_4 (280 °C), and Fe_3O_4/graphene (280 °C).

(PVDF) with a weight ratio of 80 : 10 : 10 bound in *N*-methyl-2-pyrrolidinone (NMP) (Aldrich). The slurries were coated on Cu foils and dried at 120 °C in a vacuum for 10 h to remove the solvent. Electrodes with a diameter of 10 mm were punched and weighted. The accurate mass loadings of active materials were controlled in the range of 1.45–1.65 mg cm^{-2}. 2016-type coin cells were then assembled in a glove box filled with Ar using Celgard 2400 film as separator and 1 mol L^{-1} $LiPF_6$ dissolved in a mixture of ethylene carbonate (EC), dimethyl carbonate (DMC) and ethylene methyl carbonate (EMC) with an EC : DMC : EMC volume ratio of 1 : 1 : 1 (Tianjin Jinniu Power Sources Material Co., LTD) as the electrolyte. Pure lithium foil was used as counter electrode. The charge–discharge tests were carried out on a LAND Cell Test System (2001A, Wuhan, China) between cutoff voltages of 3 V and 0.01 V. Cyclic voltammetry (CV) tests in two electrode coin-type cells were performed between 0.01 V and 3 V at a scan rate of 0.1 mV s^{-1} on a CHI760D electrochemical working station. Electrochemical impedance spectroscopy (EIS) patterns were recorded using a CHI760D electrochemical working station in the frequency range 100 kHz to 0.01 Hz with an amplitude of 5 mV.

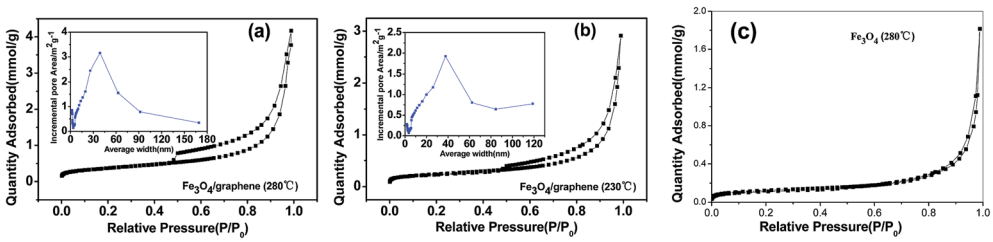

Fig. 7 The nitrogen adsorption–desorption isotherms and BJH pore size distribution curves (inset) of (a) Fe_3O_4/graphene (280 °C) composite, (b) Fe_3O_4/graphene (230 °C) composite, and (c) Fe_3O_4 nanoparticles (280 °C).

3. Results and discussion

3.1. XRD

Fig. 1 shows the XRD patterns of the as-prepared Fe_3O_4/graphene composites and pristine Fe_3O_4 nanoparticles derived from the high-temperature solvothermal process with different treatment times. From the patterns one can see that the sample obtained at a treatment temperature of 210 °C for 12 h did not show the characteristic peaks of Fe_3O_4, indicating no crystalline Fe_3O_4 formed or that the formed Fe_3O_4 particles were too small to detect. When the temperature was increased higher than 230 °C, the XRD patterns of the resultant Fe_3O_4/graphene composite and the control Fe_3O_4 nanoparticles are in good agreement with crystalline Fe_3O_4 (JCPDS, no. 19-0629). The reaction time can even be shortened to 6 h at a treatment temperature of 280 °C. No obvious diffraction peaks of graphene in the Fe_3O_4/graphene composite can be observed, indicating that the stacking of graphene sheets is disordered in these composites.[27]

3.2. FTIR spectra

Fig. 2 shows the FTIR spectra of the as-prepared Fe_3O_4 nanoparticles and Fe_3O_4/graphene composites measured in the wavelength range of 400–4000 cm^{-1}. The absorption band around 586 cm^{-1} can be assigned to Fe–O stretching vibration modes. The peak at 1108 cm^{-1} can be attributed to the skeletal C–O stretching vibration. The peak at 1620 cm^{-1} can be assigned to C=C bending vibrations of graphene. The weak peak located at 2918 cm^{-1} was ascribed to the C–H stretching vibration. The wide peak around 3440 cm^{-1} was assigned to the stretching vibration of O–H of the adsorbed H_2O. The additional peaks in curve D come from the unreacted precursors of ferrous oxalate dehydrate. This result revealed the coexistence of Fe_3O_4 and graphene in the composites and indicated also that a treatment temperature of 230 °C and a reaction time of 12 h are not enough for a complete conversion of the precursor to product.[28,29]

3.3. SEM and TEM measurements

The SEM images of graphene sheets, Fe_3O_4 nanoparticles and Fe_3O_4/graphene composites prepared at different temperatures are presented in Fig. 3. From the images it can be seen that the graphene substrate shows a stacked and crumpled morphology (Fig. 3A).[30] Interestingly, the Fe_3O_4 nanoparticles prepared solvothermally at 230 °C show a rod-like morphology with lengths of about 2 micrometers and a diameter of about 300 nm (Fig. 3B). On increasing the treatment temperature to 250 °C, was observed that the morphology of Fe_3O_4 turned into nanoparticles but mixed with a small amount of rod-like particles (Fig. 3C). At a treatment temperature of 280 °C, the resultant Fe_3O_4 particles showed only spherical morphology with diameters in the range of 30–50 nm (Fig. 3D). The comparison reveals that the morphology of the Fe_3O_4 products changed gradually from a rod-like structure to spherical particles with increasing of treatment temperature, while the particle sizes decreased. Fig. 3E shows the SEM images of the Fe_3O_4/graphene composite prepared solvothermally at 280 °C. From the SEM image it can be seen that the surface of graphene sheets was decorated tightly with Fe_3O_4 nanoparticles. For comparison, Fig. 3F gives a

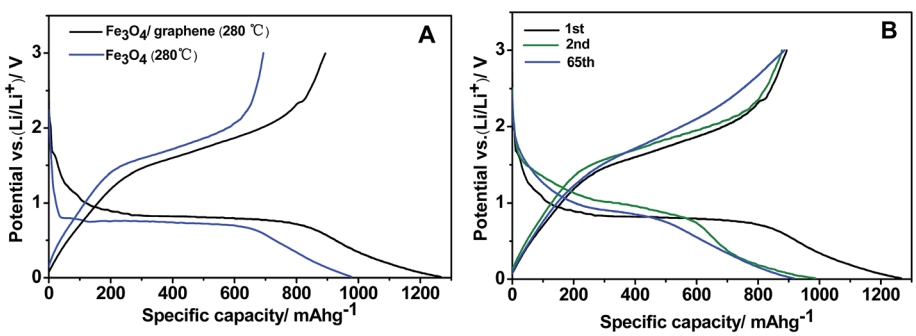

Fig. 8 (A) The first discharge–charge profiles of Fe_3O_4/graphene (280 °C) composite and that of Fe_3O_4 nanoparticles (280 °C) at a current of 0.1 C, (B) The 1st, 2nd and 65th discharge–charge profiles of Fe_3O_4/graphene (280 °C) composite at a current of 0.1 C.

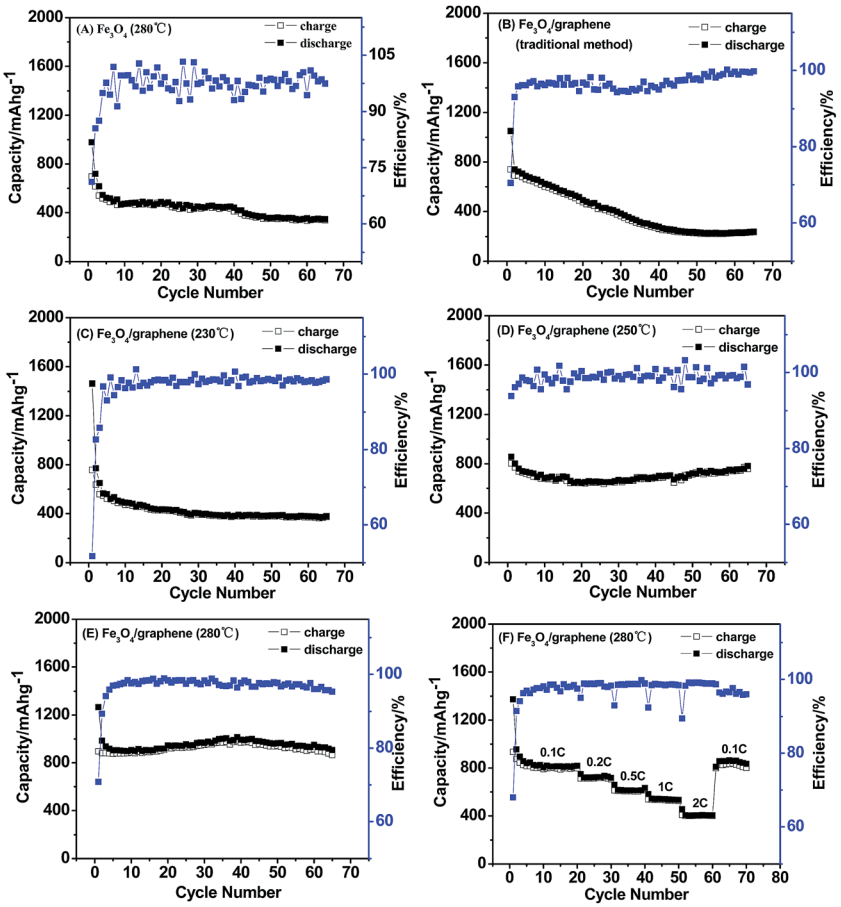

Fig. 9 Specific capabilities of different samples at a current of 0.1 C, (A) Fe_3O_4 nanoparticles (280 °C), (B) Fe_3O_4/graphene composite (traditional hydrothermal method), (C) Fe_3O_4/graphene (230 °C) composite, (D) Fe_3O/graphene composite (250 °C), (E) Fe_3O_4/graphene (280 °C), and (F) specific capabilities of Fe_3O_4/graphene (280 °C) composite at currents between 0.1–2 C.

SEM image of the Fe_3O_4/graphene composite prepared by the conventional solvothermal method, where a Teflon lined normal autoclave was used for the preparation and 200 °C was set as the maximum treatment temperature. From the SEM image it can be seen that Fe_3O_4 particles with diameter of about 250 nm are stacked on the surface of the graphene sheets. In comparison with the traditional solvothermal method, the high-temperature one can result in particles with smaller sizes, which will then lead to a high specific surface area (see Section 3.6) and better electrochemical properties (see Section 3.7).

Fig. 4 shows the TEM image of pristine graphene substrate (A) and that of the Fe_3O_4/graphene (280 °C) composite (B). The image of the graphene substrate shows clearly the layered structure with a stacked and crumpled morphology. The TEM image of the Fe_3O_4/graphene (280 °C) composite confirmed that Fe_3O_4 nanoparticles with diameter in the range of 30–50 nm were anchored on the surface of graphene sheets after the solvothermal treatment at 280 °C, which is consistent with the SEM results. The TEM image also revealed that the designed

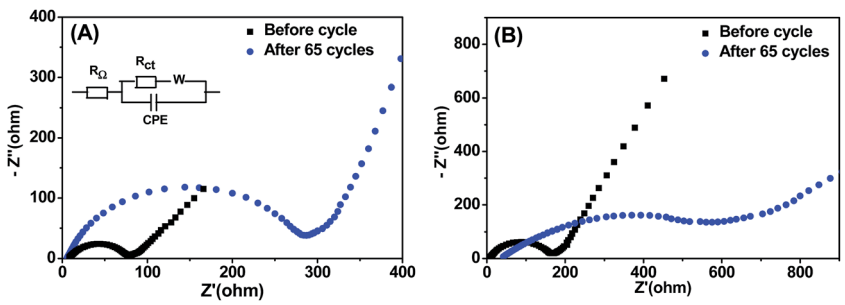

Fig. 10 AC impedance plots of (A) Fe_3O_4/graphene (280 °C) composite and (B) Fe_3O_4 nanoparticles (280 °C).

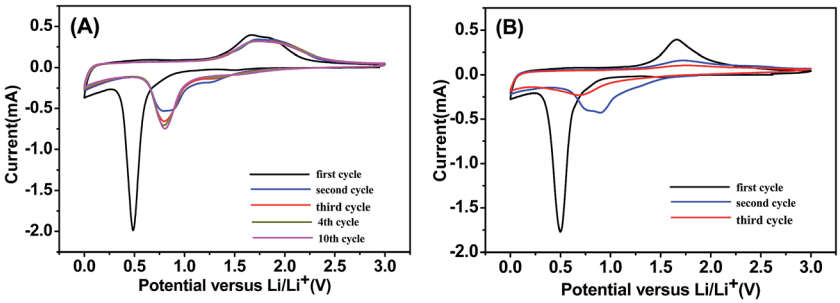

Fig. 11 Cyclic voltammograms (CV) of Fe_3O_4/graphene (280 °C) composite (A) and Fe_3O_4 nanoparticles (280 °C) (B).

structure can prevent the aggregation of Fe_3O_4 nanoparticles effectively.[31–34]

3.4. Raman spectra

Curves A and B in Fig. 5 exhibit the Raman spectra of pristine graphene substrate and that of the Fe_3O_4/graphene (280 °C) composite, respectively. The two peaks at 1332 and 1561 cm^{-1} in curve A can be assigned to the D and G bands for carbon.[35,36] The G band corresponds to sp^2 hybridized carbon, while the D band can be attributed to the presence of sp^3 defects within the carbon. Curve B also possesses D and G bands with peaks at 1334 and 1575 cm^{-1}, respectively. For the Fe_3O_4/graphene composites, the intensity ratio of the D to G bands (I_D : I_G) was calculated to be 1.004, which is higher than that of the pristine graphene substrate (0.926). The change of intensity ratio of the D and G bands could be ascribed to the exfoliation of graphene and the presence of Fe_3O_4 nanoparticles between graphene sheets.[37,38]

3.5. Thermal analysis

Fig. 6 shows the typical TGA profiles of the as-prepared Fe_3O_4/graphene composite, Fe_3O_4 particles and pristine graphene, respectively. For the Fe_3O_4/graphene composite, the weight loss of 0.7% between room temperature and 200 °C can be attributed to the loss of adsorbed water. The weight gain between 200 to 450 °C was caused by the oxidation of Fe_3O_4. For pure Fe_3O_4, a weight gain of 5.0% was detected, which is close to the theoretical calculation of 3.5%. The pristine graphene showed a drastic weight loss between 480 and 550 °C, while the Fe_3O_4/graphene composite presented an obvious weight loss in the range of 560 to 660 °C. The variation of temperature range of weight loss for pristine graphene and Fe_3O_4/graphene composite can be explained by the Fe_3O_4 anchored tightly onto the surface of the graphene layers retarding the oxidation rate of the graphene substrate. The weight percentages of carbon and Fe_3O_4 in the Fe_3O_4/graphene composite were approximately 12.9% and 87.1% as derived from the weight losses of graphene and the mass gains of the oxidation of Fe_3O_4–Fe_2O_3. Theoretical contents of 7.4% and 92.6%, respectively, for graphene and Fe_3O_4 can be deduced based on the quantity of the applied precursors. The detected carbon content in the composite based on the TGA results is a little bit higher than the theoretical value. The difference between them can be attributed to the composition character of the Fe(II) oxalate precursor, which could introduce *in situ* amorphous carbon to the composites *via* decomposition of the oxalate moieties during the high temperature solvothermal treatment.

3.6. Nitrogen adsorption–desorption measurements

N_2 adsorption–desorption isotherms were employed to investigate specific surface area and porosity of the Fe_3O_4/graphene composites prepared at different temperatures and that of the Fe_3O_4 nanoparticles. As can be seen, the isotherms of the Fe_3O_4/graphene composites showed very obvious hysteresis loops and capillary condensation steps (Fig. 7(a) and (b)), suggesting the existence of porous structure in them.[39] In comparison with the composites, Fe_3O_4 nanoparticles showed a narrow and irregular hysteresis loop and the capillary condensation steps shifted to a higher relative pressure, implying a reduction of porosity.[40] The BJH pore size distributions at around 39 nm and 38 nm, respectively, for Fe_3O_4/graphene (280 °C) and Fe_3O_4/graphene (230 °C) composites were calculated. But no uniform pore size in the pristine Fe_3O_4 nanoparticles can be detected. The pore size distribution data of the samples, which were calculated from the desorption branch of the isotherms using the BJH algorithm, further supported the speculation deduced from the isothermal curve analysis. The pores in the Fe_3O_4/graphene composite could alleviate the volume changes of the Fe_3O_4 nanoparticles during the lithium ion insertion/desertion process, which would lead to stable electrochemical performance (see Section 3.7). The calculated BET specific surface areas are 30, 19 and 10 m^2 g^{-1}, respectively, for the above mentioned three samples. The large specific surface area of the Fe_3O_4/graphene (280 °C) composite can be attributed to the integration of graphene sheets with the nano-sized Fe_3O_4 particles. The increase of specific surface area for the Fe_3O_4/graphene composite prepared at high temperatures can be attributed to the difference of particle size. The smaller the particles sizes, the higher specific surface area could be deduced. The N_2 adsorption–desorption measurements are consistent with the SEM and TEM observations (see Section 3.3).

3.7. Electrochemical properties

Fig. 8(A) shows the initial charge–discharge voltage profiles of the Fe_3O_4/graphene (280 °C) composite and Fe_3O_4

nanoparticles at 0.1 C (92.6 mA g^{-1}). The first discharge voltage profile of the Fe_3O_4/graphene composite is very similar to that of Fe_3O_4 nanoparticles. Both of them presented a steep voltage drop from about 2.5 to 0.85 V, which can be attributed to the reaction of $Fe_3O_4 + xLi^+ + xe^- \leftrightarrow LixFe_3O_4$.[41] Then the Fe_3O_4/graphene composite electrode showed a long discharge plateau potential around 0.85 V, which is due to the reduction of Fe ions to form nano-sized metallic Fe and amorphous Li_2O through a conversion reaction.[42] The sloping curve of the Fe_3O_4/graphene composite from about 0.83 to 0.01 V could be attributed to the formation of a solid electrolyte interface (SEI) film and the reversible reaction between lithium and graphene sheets $2C + Li^+ + e^- \leftrightarrow LiC_2$.[43–45] The initial discharge and charge capacities of the Fe_3O_4/graphene composites were estimated to be 1266 and 897 mA h g^{-1}, respectively, which are higher than those of the electrode made of pristine Fe_3O_4 nanoparticles (978.5 and 697 mA h g^{-1}). Fig. 8(B) shows the 1st, 2nd and 65th discharge–charge profiles of an electrode made of Fe_3O_4/graphene (280 °C) composite at 0.1 C. A reversible capacity of 907 mA h g^{-1} was retained at 0.1 C even after 65 discharge–charge cycles. This confirms that graphene with outstanding intrinsic properties can effectively improve the electrochemical performance of transition metal oxides.

Fig. 9 shows the reversible capacity *versus* cycle number for Fe_3O_4 nanoparticles and Fe_3O_4/graphene composites prepared at different temperatures. The reversible capacity of pristine Fe_3O_4 nanoparticles faded quickly and showed a low capacity of only 346 mA h g^{-1} after 65 cycles (Fig. 9A). For the Fe_3O_4/graphene composites, it can be seen that with the increase of treatment temperature, the reversible capacities had obviously increased values. For the resultant composites at 230, 250 and 280 °C, capacities of about 378, 781 and 907 mA h g^{-1}, respectively, were retained after 65 charge–discharge cycles. Their coulombic efficiencies remained more than 95%. On increasing the treatment temperature further to 310 °C, no obvious improvement to the electrochemical performance of the resultant composite was observed. Therefore, 280 °C has been selected as the preferred treatment temperature based on energy consumption considerations. The control Fe_3O_4/graphene composite prepared by the conventional solvothermal method, exhibited a low capacity of 230 mA h g^{-1} after 65 cycles, which is much lower than that delivered by the Fe_3O_4/graphene composites prepared *via* the high-temperature solvothermal processes and is even lower than that of the pristine Fe_3O_4 nanoparticles (280 °C). The theoretical weight percentage of the integrated graphene in our case is 7.4%, which is much lower than the reported data and will be of benefit to the commercialization of the Fe_3O_4/graphene composite.[17,19,27] There are several cycles showing capacity higher than the theoretical one, which may be due to the Li^+ trapped both in the interlayer of carbons and cavities, as proposed by Tokumitsu *et al.*[46] The excellent capacity retention can be ascribed to the existence of graphene in the composites that can improve the electrical conductivity of the composite and can also accommodate the volume change of Fe_3O_4 nanoparticles during the repetitive Li^+ insertion–extraction cycling.[47,48] The capacity variation among the different composites can be contributed to by the differences of morphology, particle size and crystal perfection of the Fe_3O_4 particles in them derived at different temperature by the solvothermal synthesis. The remarkable high-rate capability of Fe_3O_4/graphene (280 °C) is demonstrated in Fig. 9F. And reversible capacities of about 830 mA h g^{-1} at 0.1 C, 720 mA h g^{-1} at 0.2 C, 615 mA h g^{-1} at 0.5 C, 540 mA h g^{-1} at 1 C and 410 mA h g^{-1} at 2 C were delivered by this composite electrode. The reversible capacity returned to its original value as the current rate reduces back, revealing the superior reversibility of this composite electrode and its suitability as a high rate anode material.

To illustrate further the differences between Fe_3O_4 nanoparticles and Fe_3O_4/graphene (280 °C) composite, electrochemical impedance spectroscopy (EIS) measurements were carried out based on electrodes made of them in the frequency range from 10^5 to 0.01 Hz before or after testing the galvanostatic cycles, and typical Nyquist plots are given in Fig. 10. The EIS was also simulated by Z-view software using the equivalent circuit as shown in Fig. 10. In the equivalent circuit (inset), R_Ω and R_{ct} are the ohmic resistance (total resistance of the electrolyte, separator, and electrical contacts) and the charge transfer resistance, respectively. CPE is the constant phase element and represents double layer capacitance, and W represents the Warburg impedance, reflecting the solid-state diffusion of Li ions into the bulk of the active materials. The Nyquist plots for the samples before and after cycling are similar, displaying a depressed semicircle in the high-middle frequency region, which could be assigned to the charge transfer resistance (R_{ct}), and an inclined line in the low frequency region, which represents the Warburg impedance.[49,50] It can be seen from the image that the diameter of the semicircle for Fe_3O_4/graphene (280 °C) before the cycle is much smaller than that of Fe_3O_4 nanoparticles, indicating a lower charge transfer resistance of the material.[51] It is believed that the graphene existing in the system was responsible for the lower charge transfer resistance of the composite material. After 65 cycles, it is worth noting that the diameter of the semicircles was enlarged for both the samples. However, the lowest charge-transfer resistance was obtained again on Fe_3O_4/graphene electrode. The results confirmed that the existence of graphene significantly enhanced the conductivity of the electrode made of Fe_3O_4/graphene composite.

The cyclic voltammogram (CV) of the as-synthesized Fe_3O_4/graphene (280 °C) composite was collected over the potential range from 0.01 to 3.0 V at a scan rate of 0.1 mV s^{-1}. As shown in Fig. 11(A) in the first cycle two peaks at 0.01 and 0.49 V, respectively, were observed for the cathodic process, which are ascribed to the lithiation reaction of $Fe_3O_4 + 8Li^+ + 8e^- \leftrightarrow 3Fe^0 + 4Li_2O$ and $2C + Li^+ + e^- \leftrightarrow LiC_2$.[52] While two peaks at about 1.68 and 1.89 V were recorded in the anodic process, which correspond to the oxidation of Fe^0 to Fe^{2+} and Fe^{3+} during the anodic process. During the subsequent cycles, both the cathodic and anodic peak potentials shift to high voltage ranges due to the polarization of electrode materials in the first cycle and the formation of the SEI film. Thereafter, the peak intensity tended to a constant and kept stable finally, implying good cycling stability. On the contrary, as shown in Fig. 11(B), the peak

intensity and integral areas of the CV curves in the first three cycles decreased obviously for Fe_3O_4 nanoparticles, implying poor capacity retention ability. The results are also agreed well with the constant current discharge and charge processes testing.

4. Conclusions

Fe_3O_4/graphene composite anode materials with excellent electrochemical properties have been prepared by the one-step solvothermal method at elevated temperature (up to 310 °C) using an organic iron salt as precursor. On increasing the treatment temperature from 230 to 280 °C, the morphologies of the resultant Fe_3O_4 particles turned from tubes with lengths of about 2 micrometers and diameters of about 300 nm to nanoparticles with diameters in range of 30–50 nm. In comparison with the traditional solvothermal method (<240 °C), the high-temperature one can provide Fe_3O_4 nanocrystals in a short treatment time (only 6 h), meanwhile, the resultant Fe_3O_4/graphene composite could deliver higher capacity and better cycling performance than that derived from the traditional solvothermal process. Control experiments revealed that the Fe_3O_4/graphene composites prepared at 280 °C possessed the best electrochemical performance, and a high capacity of 907 mA h g^{-1} could be retained after 65 cycles at a current density of 0.1 C (92.6 mA g^{-1}). This strategy which employs graphene (<10% weight percentages) as supporting sheets for loaded metal oxide achieved by the one-step high-temperature solvothermal process was demonstrated to be an effective way to improve the specific capacity and the cycling performance of metal oxide anode materials for lithium ion batteries. The excellent electrochemical performance of the Fe_3O_4/graphene composites resulting from the high-temperature solvothermal process can be related to the enhancement of conductivity by the graphene sheets and the nano-scaled crystalline Fe_3O_4 particles. The high temperature could result in Fe_3O_4 nanocrystals with more perfect structure and enhance the important interfacial interaction between the graphene substrate and the Fe_3O_4 nanocrystals (30–50 nm). Furthermore, the graphene substrates distributed among the Fe_3O_4 nanoparticles can prevent the aggregation of the Fe_3O_4 particles and can also provide a void against the volume changes of Fe_3O_4 nanoparticles during the charge–discharge process. This high-temperature solvothermal method does not need a long reaction time and separate calcinations as usually required in the traditional method. This constitutes a facile approach to the synthesis of transition metal oxide/graphene composites with good cycling performance and high capacity retention as anode materials for lithium-ion batteries. We expect that the methodology presented herein will be also useful for the preparation of other kinds of electrode materials for LIBs.

Acknowledgements

This work is supported by the National Key Project on Basic Research (Grant no. 2012CB722705), the National High Technology Research and Development Program of China (no. 2012AA110407 and 2014AA052303) and the Natural Science Foundation of China (no. 21103096 and U1232104). Y. Q. Wang would like to thank the financial support from the Top-notch Innovative Talent Program of Qingdao City (Grant no. 13-CX-8) and the Taishan Scholar Program of Shandong Province.

References

1 M. R. Palacin, *Chem. Soc. Rev.*, 2009, **38**, 2565–2575.
2 M. Armand and J. M. Tarascon, *Nature*, 2008, **451**, 652–657.
3 F. Cheng, Z. Tao, J. Liang and J. Chen, *Chem. Mater.*, 2008, **20**, 667–681.
4 X. P. Gao and H. X. Yang, *Energy Environ. Sci.*, 2010, **3**, 174–189.
5 J. Qu, Y. X. Yin, Y. Q. Wang, Y. Yan, Y. G. Guo and W. G. Song, *ACS Appl. Mater. Interfaces*, 2013, **5**, 3932–3936.
6 Y. Sun, X. Hu, W. Luo, F. Xia and Y. Huang, *Adv. Funct. Mater.*, 2013, **23**, 2436–2444.
7 S. K. Behera, *J. Power Sources*, 2011, **196**, 8669–8674.
8 J. Liu, Y. Zhou, F. Liu, C. Liu, J. Wang, Y. Pan and D. Xue, *RSC Adv.*, 2012, **2**, 2262–2265.
9 Q. Q. Xing, J. P. Tu, Y. Lu, J. Chen, Y. X. Yu, Y. Q. Qiao, X. L. Wang and C. D. Gu, *J. Phys. Chem. C*, 2012, **116**, 6495–6502.
10 Y. Chen, H. Xia, L. Lu and J. Xue, *J. Mater. Chem.*, 2012, **22**, 5006–5012.
11 W. M. Zhang, X. L. Wu, J. S. Hu, Y. G. Guo and L. J. Wan, *Adv. Funct. Mater.*, 2008, **18**, 3941–3946.
12 Y. He, L. Huang, J. S. Cai, X. M. Zheng and S. G. Sun, *Electrochim. Acta*, 2010, **55**, 1140–1144.
13 T. Muraliganth, A. V. Murugan and A. Manthiram, *Chem. Commun.*, 2009, 7360–7362.
14 G. H. Lee, J. G. Park, Y. M. Sung, K. Y. Chung, W. I. Cho and D. W. Kim, *Nanotechnology*, 2009, **20**, 295205–295209.
15 A. K. Geim and K. S. Novoselov, *Nat. Mater.*, 2007, **6**, 183–191.
16 A. K. Geim, *Nature*, 2009, **324**, 1530–1534.
17 X. Li, X. Huang, D. Liu, X. Wang, S. Song, L. Zhou and J. Zhang, *J. Phys. Chem. C*, 2011, **115**, 21567–21573.
18 D. Chen, G. Ji, Y. Ma, J. Y. Lee and J. Lu, *ACS Appl. Mater. Interfaces*, 2011, **3**, 3078–3083.
19 Y. Liu, K. Huang, H. Luo, H. Li, X. Qia and J. Zhong, *RSC Adv.*, 2014, **4**, 17653–17659.
20 P. Lian, X. Zhu, S. Liang, Z. Li, W. Yang and H. Wang, *Electrochim. Acta*, 2010, **55**, 3909–3914.
21 S. M. Paek, E. J. Yoo and I. Honma, *Nano Lett.*, 2009, **9**, 72–75.
22 S. L. Chou, J. Z. Wang, M. Choucair, H. K. Liu, J. A. Stride and S. X. Dou, *Electrochem. Commun.*, 2010, **12**, 303–306.
23 M. Zhang, M. Jia and Y. Jin, *Appl. Surf. Sci.*, 2012, **261**, 298–305.
24 T. Wang, X. Wang, Y. Lu, Q. Xiong, X. Zhao, J. Cai, S. Huang, C. Gu and J. Tu, *RSC Adv.*, 2014, **4**, 322–330.
25 G. Zhou, D. W. Wang, F. Li, L. Zhang, N. Li, Z. S. Wu, L. Wen, G. Q. Liu and H. M. Cheng, *Chem. Mater.*, 2010, **22**, 5306–5313.
26 Q. Yu, A. Fu, H. Li, H. Liu, R. Lv, J. Liu, Z. Guo and X. S. Zhao, *Colloids Surf., A*, 2014, **457**, 288–296.

27 P. Lian, X. Zhu, H. Xiang, Z. Li, W. Yang and H. Wang, *Electrochim. Acta*, 2010, **56**, 834–840.
28 C. Nethravathi and M. Rajamathi, *Carbon*, 2008, **46**, 1994–1998.
29 Y. Liang, D. Wu, X. Feng and K. Mullen, *Adv. Mater.*, 2009, **21**, 1679–1683.
30 J. C. Meyer, A. K. Geim, M. I. Katsnelson, K. S. Nosvoselov, T. J. Booth and S. Roth, *Nature*, 2007, **446**, 60–63.
31 Z. S. Wu, W. Ren, L. Wen, L. Gao, J. Zhao, Z. Chen, G. Zhou, F. Li and H. M. Chen, *ACS Nano*, 2010, **6**, 3187–3194.
32 P. Lian, X. Zhu, S. Liang, Z. Li, W. Yang and H. Wang, *Electrochim. Acta*, 2011, **56**, 4532–4539.
33 X. Huang, X. Zhou, K. Qian, D. Zhao, Z. Liu and C. Yu, *J. Alloys Compd.*, 2012, **514**, 76–80.
34 Y. Dong, R. Ma, M. Hu, H. Cheng, Q. Yang, Y. Y. Li and J. A. Zapien, *Phys. Chem. Chem. Phys.*, 2013, **15**, 7174–7181.
35 B. Zhao, G. Zhang, J. Song, Y. Jiang, H. Zhuang, P. Liu and T. Fang, *Electrochim. Acta*, 2011, **56**, 7340–7346.
36 C. Zhang, X. Peng, Z. Guo, C. Cai, Z. Chen, D. Wexler, S. Li and H. Liu, *Carbon*, 2012, **50**, 1897–1903.
37 J. Su, M. Cao, L. Ren and C. Hu, *J. Phys. Chem. C*, 2011, **115**, 14469–14477.
38 P. Poizot, S. Laruelle, S. Grugeon, L. Dupont and J. M. Tarascon, *Nature*, 2000, **407**, 496–499.
39 R. R. Xu, W. Q. Pang, J. H. Yu and J. S. Chen, *Chemistry-Zeolites, and Porous Materials*, Science Press, Beijing, 2004, pp. 146–147.
40 H. Li, J. Sang, J. Zhao, A. Fu, H. Liu, M. Xu, G. Pang and X. S. Zhao, *New J. Chem.*, 2012, **36**, 2308–2315.
41 C. Ban, Z. Li, Z. Wu, M. J. Kirkham, L. Chen and Y. S. Jung, *Adv. Energy Mater.*, 2011, **1**, 58–62.
42 J. Z. Wang, C. Zhong, D. Wexler, N. H. Idris, Z. X. Wang, L. Q. Chen and H. K. Liu, *Chem.–Eur. J.*, 2011, **17**, 661–667.
43 S. Wang, J. Zhang and C. Chen, *J. Power Sources*, 2010, **195**, 5379–5381.
44 D. Pan, S. Wang, B. Zhao, M. Wu, H. Zhang, Y. Wang and Z. Jiao, *Chem. Mater.*, 2009, **21**, 3136–3142.
45 C. Lei, F. Han, Q. Sun, W. C. Li and A. H. Lu, *Chem.–Eur. J.*, 2014, **20**, 139–145.
46 K. Tokumitsu, H. Fujimoto, A. Mabuchi and T. Kasuh, *Carbon*, 1999, **37**, 1599–1605.
47 C. Wu, Q. Zhuang, Y. Wu, L. Tian, Y. Cui and X. Zhang, *Mater. Lett.*, 2013, **113**, 1–4.
48 W. Wei, S. Yang, H. Zhou, I. Lieberwirth, X. Feng and K. Mullen, *Adv. Mater.*, 2013, **25**, 2909–2914.
49 D. Zhang, Y. J. Mai, J. Y. Xiang, X. H. Xia, Y. Q. Qiao and J. P. Tu, *J. Power Sources*, 2012, **217**, 229–235.
50 B. Wang, G. Wang, Z. Zheng, H. Wang, J. Bai and J. Bai, *Electrochim. Acta*, 2013, **106**, 235–243.
51 C. Wang, H. Li, A. Fu, J. Liu, W. Ye, Z. Guo, S. Pang and X. S. Zhao, *New J. Chem.*, 2014, **38**, 616–623.
52 L. Wang, Y. Yu, P. C. Chen, D. W. Zhang and C. H. Chen, *J. Power Sources*, 2008, **183**, 717–723.